Improving ATMS Remapping Accuracy Using Adaptive Window and Noise-tuning Method in Backus-Gilbert Inversion

Jun Zhou[1], Hu Yang[1*], Robbie Iacovazzi[2]

1. Earth System Science Interdisciplinary Center, University of Maryland, College Park, MD 20740, USA;
2. Global Science and Technology Incorporated, 7855 Walker Drive, Suite 200, Greenbelt, MD 20770, USA

The final version is submitted to

IEEE Trans. Geo. Remote Sensing

June 9th, 2022

* Earth System Science Interdisciplinary Center, University of Maryland, 5825 University Research Court, Suite 4001, College Park, Maryland 20740-3823, USA. Email: huyang@umd.edu. Phone number: 443-917-8848

Abstract

One of the data fusion issues for observations from multiple space-borne microwave sensors is the non-uniform spatial resolution. Although the Backus-Gilbert Inversion (BGI) algorithm has long been used for the Advanced Technology Microwave Sounder (ATMS) antenna pattern matching, previous studies showed that it has difficulty in accurate remapping from the coarser to the finer observations. Since BGI tends to enhance the data's high spatial frequency components including both information and noise, it is a challenge to increase the spatial resolution while maintaining an acceptable noise level. This study unveils that the main cause of this issue is the insufficiency of the information provided by the conventional fixed reconstruction window. An adaptive window method is applied to provide sufficient information for the reconstruction at each scan position. In addition, a new noise tuning method is proposed to eliminate the scan-angle-dependent features in the noise caused by the sensor's cross-track scanning manner. Results from simulations and NOAA ATMS data show that compared to the fixed window, the new method can significantly reduce the bias stemming from the resolution difference. The issue of the deterioration of the resolution enhancement capability near the scan edge in the fixed window method has been largely ameliorated. The overall Root-Mean-Square error is declined by 30%. The new noise tuning method is capable of suppressing the noise level at around 0.6 K over scan.

Keywords: ATMS, Backus–Gilbert Inversion, Data fusion, Remapping, Spatial resolution enhancement

I. INTRODUCTION

Satellite passive microwave observations have significant value in atmospheric remote sensing, numerical weather predictions (NWP) as well as climate modeling. However, due to the limited size of the antenna reflector and the different observation frequencies, the measurements from different channels and sensors often have nonuniform spatial resolution. This has become a critical issue, since for many applications a consistent spatial resolution for measurements from multiple data sources is expected. The techniques using combined data sets are not strictly valid unless steps are taken to match data with different spatial resolution [1].

There are two different approaches to unify the spatial resolution of observations from different data sources. One is the conversion of the swath-based measurements to a regular Earth-centered grid, equivalent to antenna pattern deconvolution [2]-[5]. The other is the matching of antenna pattern, which makes estimation of the antenna temperature (Ta) the sensors would have measured with the prescribed target antenna pattern [1][6][7]. In both methods, if the generated measurements have finer (coarser) spatial resolution than the raw data, this process is also known as spatial resolution enhancement (degradation). In this study, we will focus on the algorithms based on antenna pattern matching.

The Backus-Gilbert Inversion (BGI) algorithm and the Fourier filtering [8] are currently available analytical algorithms for microwave data remapping. The early research works on the BGI laid out a rigorous mathematical basis for the inversion of the seismic

observations to produce detailed profiles of the earth's density structure [9]-[11]. Later, Stogryn [2] applied it to the specific problem of microwave footprint manipulation. This work formed the basis of the development of some computationally efficient versions [12]-[14]. The BGI algorithm has been widely applied to multi-frequency microwave radiometers for spatial resolution matching, such as the Special Sensor Microwave/Imager, the Microwave Radiation Imager (MWRI), and the Advanced Technology Microwave Sounder (ATMS) [1][6][15]. It has been implemented in the ATMS operational resampling algorithm to produce ATMS measurements at each Cross-track Infrared Sounder (CrIS) Field of View (FOV) [16]. The Fourier filtering algorithm, manipulating the antenna pattern in frequency domain, also has applications in ATMS and MWRI data remapping [17]-[18]. The comparison of the BGI and the Fourier filtering algorithms [7] showed that the former has higher remapping accuracy than the latter one in both resolution enhancement and degradation. In recent years, various Convolutional Neural Networks have been designed for spatial resolution enhancement for microwave sensors, such as the MWRI onboard Fengyun-3 series of satellites [19] - [23].

In our previous study [6]-[7], the BGI algorithm has been applied to remap from ATMS channel 1 (23 GHz) with 5.2° beam width and channel 3 (50 GHz) with 2.2° beam width to a proxy AMSU-A 3.3° FOV size. It shows that while the results for resolution degradation are encouraging, the resolution enhancement the algorithm can achieve is quite limited. The enhancement procedure narrows the beam width only by 15%. The comparison between the reconstructed image and the simulated truth shows large bias

around coastlines and hurricane centers. Other researchers also found the same issue when the BGI was used to match the spatial resolution of the SSM/I 19 GHz and 22 GHz channels to its 37 GHz channel [1]. Since the resolution enhancement is usually achieved at the cost of the amplification in noise, it is a challenge to further increase the spatial resolution for these lower frequency channels while maintaining their noise at an acceptable level.

In this study, the ATMS spatial resolution enhancement accuracy is improved by using the adaptive window and a new noise-tuning method. In BGI, the reconstruction window is a key parameter to determine which source observations are to be used to produce the target ones. In the past, a fixed square-shaped window was commonly adopted for all scan positions [1][6][7]. Our most recent work [24] found that for spatial resolution enhancement, utilizing more observations with overlapping FOVs might be the key to increase the remapping accuracy. In this paper, the adaptive window is applied in BGI to provide sufficient information for the spatial resolution enhancement. The noise-tuning parameter is another key parameter in BGI. It controls the tradeoff between the spatial resolution and the noise. Our study found that a fixed value of this parameter for all the scan positions, as used in previous studies [1][3][5][28], led to a FOV-dependent feature in noise. To address this issue, a new noise-tuning method is proposed to ensure a stable and acceptable noise level in the reconstructed dataset. The new algorithm will be used to determine the optimum remapping coefficients, which converts ATMS observations from 5.2° FOV to a consistent AMSU-A 3.3° FOV.

The remainder of this paper is organized into four sections. Section II describes the adaptive reconstruction window and the new noise-tuning method. Section III employs simulations to determine the optimum parameters and quantitatively evaluate the synthetic point spread function (PSF) and the remapping results. The new method is applied to real ATMS observations in Section IV. Summary and conclusions are provided in Section V.

II. IMPROVEMENTS TO BGI REMAPPING ALGORITHM

This study focuses on improving the ATMS resolution enhancement accuracy by optimizing the reconstruction window and the noise tuning parameter in BGI algorithm. Before diving into the new method in the next two subsections, the BGI algorithm will be briefly introduced.

Ignoring the scan-motion smearing caused by the continuous scan mode of the ATMS, the antenna temperature (Ta) at a location (ρ_0) can be expressed as the convolution of the scene brightness temperature (Tb) with the antenna gain function (G) projected onto Earth surface, i.e. point spread function (PSF) [8]:

$$Ta(\rho_0) = \int Tb(\rho) \cdot G(\rho_0, \rho) dA \tag{1}$$

G is normalized so that $\int_{4\pi} G \ d\Omega = 1$. Following previous research, the antenna gain function in (1) is modeled by a two-dimensional Gaussian function with 3-dB (half-power) point that matches the footprint size [5][25]. The BGI algorithm aims at finding a set of coefficient values (a_i) that provide a linear combination of the source

measurements (Ta_{source}) at each of their locations (ρ_i) to estimate a target observation with the target antenna pattern (Ta_{target}):

$$Ta_{target}(\rho_0) = \sum_{i=1}^{n} a_i Ta_{source}(\rho_i) \quad (2)$$

Assuming an independent and constant noise variance σ^2_{source} for all observations, noise in the target observations can be expressed as:

$$\sigma^2_{target} = \sigma^2_{source} \sum_{i=1}^{n} a_i^2 \quad (3)$$

To reach a tradeoff between the resolution enhancement and the noise suppression, the optimal coefficients (a_i) are derived by minimizing the following objective function Q:

$$Q = Q_0 \cos\gamma + \sigma^2_{target} w \sin\gamma \quad (4a)$$

$$Q_0 = \int \left(\sum_{i=1}^{n} a_i G_{source}(\rho_i, \rho) - G_{target}(\rho_0, \rho) \right)^2 dA \quad (4b)$$

G_{source} and G_{target} are the source and target antenna gain functions. Q_0 is the fit error, measuring the mismatch between the reconstructed antenna gain and the target one. σ^2_{target} denotes the noise in the reconstructed antenna temperature. Both terms contribute to the remapping errors. The parameter w is set to 0.001 to make the two terms numerically compatible. The parameter γ is a tradeoff factor that places degrees of emphasis on either the antenna pattern match or the noise suppression in the estimates of Ta_{target}. Larger value of γ puts more penalty on noise and thus produce lower noise but higher mismatch in antenna pattern. While smaller value of γ puts more penalty on fit error and thus produce better match in antenna pattern but higher noise. With an appropriately selected γ, minimizing the objective function gives a

series of coefficients that can produce the dataset with desired antenna pattern match and acceptable noise level. The way to determine this parameter will be elaborated in section II-B. To reduce the impact of the geometric deformation of the FOVs over the scan caused by the cross-scanning manner of the sensors, the optimum coefficients are derived for each FOV position. Given the radiometer configuration, the coefficients need to be determined only once, and the inversion procedure reduces to a weighted sum of the measurements (2) [6][7][16]. The detailed description of the algorithm and the solution of the coefficients can be found in [1][26][27].

A. Adaptive Reconstruction Window

In the BGI algorithm, the target antenna temperature is generated as a weighted linear sum of measurements within a certain reconstruction window. For the intrinsic antenna pattern matching, this window is usually set to be a fixed one for all the scan positions. In the experiments of [2], the window is selected to be 3, 5, and 7 along one scan line. Robinson et al. [1] used a fixed square window, 3×3, 5×5, and 7×7 to enhance and match the resolution of the measurements of SSM/I. Bennartz [29] used a 7×7 set for the optimal convolution of AMSU-B to AMSU-A. For the footprint matching from ATMS channel 1 with 5.2° beam width to AMSU-A like 3.3° beam width, the reconstruction window is fixed to 3×3 [6]-[7]. This fixed 3×3 is also adopted in the ATMS operational resampling algorithm to remap ATMS observations at CrIS FOVs [16].

Some researchers used a more flexible window that varies along scan line. This kind of reconstruction window determines only the source samples adjacent to the target FOV are included in the remapping. The degree of adjacency is measured in terms of the distance [30], the elevation angle [28] or the volume of the overlap [31] between the source FOV and the target FOV. To avoid the numerical problems in the matrix-inversion step of BGI, Long and Daum [3] adopted the observations in the reconstruction only if their relative antenna gain at the pixel of interest is greater than a specific threshold. Different thresholds have been selected for specific sensors and for specific resolution enhancement purposes. For example, the gain threshold is set to -11 dB for SSM/I and later adjusted to -8 dB for more sensors in the NASA-sponsored Calibrated Passive Microwave Daily Equal-Area Scalable Earth Grid 2.0 Brightness Temperature (CETB) Earth System Data Record [3]-[5]. So far, this kind of reconstruction window was mostly used in antenna pattern deconvolution. In our preliminary experiment, this adaptive window was applied to ATMS remapping from beam width 5.2° to 1.1° and the result showed that the noise level can be significantly reduced [24]. This initial study shed light on the advantage of the adaptive window, but left some key questions that need to be further addressed, such as how to objectively determine the optimum window and other parameters in BGI.

In this study, the adaptive window defined in Long and Daum [3] will be applied to the ATMS intrinsic antenna pattern remapping from beam width 5.2° to 3.3° which is required in the ATMS operational resampling process [8, 16]. The objective methods to determine the optimum adaptive window and other key parameters will be

thoroughly discussed and presented. To apply the adaptive window method, both the source and target antenna patterns need to be projected onto earth surface. In previous studies regarding ATMS remapping, the projection is made with 2.5 times the sensor's -3 dB beam width [6][7][16], since the antenna pattern within such solid angle includes the main beam and contains major part of the total beam energy [32]. In this study, in order to compare the source, synthetic and target PSFs over the same area later in Section III. C, the target and the source antenna patterns are projected with the same zenith angle range. Specifically, the source antenna pattern is projected with 2.5 times its beam width (5.2°) while that factor for the target antenna pattern with 3.3° beam width is $\frac{2.5\times5.2^\circ}{3.3^\circ} = 3.9$. Our research found that projecting the antenna pattern with larger zenith angle won't result in much difference in the remapping results. Based on the projected antenna patterns, the overlap between each source antenna pattern and the target one is determined. The observations whose maximum antenna gain within the pixel of interest exceeds a certain threshold value are adopted in the reconstruction. This threshold is expressed in terms of decibel below the peak gain of the antenna pattern. Fig. 1 illustrates an adaptive window with the gain threshold of -5 dB versus the fixed 3×3 window. The red and black crosses respectively represent the source ATMS channel-1 5.2° FOV centers within the 3×3 window and the adaptive window. The pixel of interest, i.e. the outline of the projection of the target antenna pattern with 3.9 times its -3 dB beam width is represented by the blue circles and its center coincides at the center of the 3×3 window. To keep the integrity of the 3×3 window, the first and the last FOVs of ATMS scan lines are excluded from the

following discussion. Unlike the 3×3 window fixed for all ATMS FOVs, the adaptive window varies along the scan positions and maximizes the use of available source observations. Considering the fact that the optimum threshold of the adaptive window is determined by the source and target gain patterns and sampling geometry, its value should vary among different channels and sensors. In Section III, the optimum threshold for ATMS remapping window will be objectively selected through simulations.

B. A New Noise-tuning Method

According to the objective function (4), the noise-tuning parameter γ controls the tradeoff between the resolution and the noise. In previous studies, a fixed γ is selected to maximize the correlation between the resolution enhanced results and the target references, which can be either the simulated truth or the real observations with finer spatial resolution but higher observation frequencies [1][3][5][28]. However, this strategy could cause a problem in the antenna pattern remapping for a cross-track scanning sensor like ATMS.

Equation (4) indicates that the noise and fit error are the two factors that contribute to the remapping error. As will be showed in Section III-D, with the adaptive window, the noise, rather than the fit error, plays a major role in the remapping uncertainty. Due to the ATMS's cross-track scanning manner, the FOV size at nadir is much smaller than that at scan edge. This enables the reconstruction at nadir to achieve higher spatial resolution than at edge. As BGI tends to enhance the high frequency components in

signal including both information and noise, the noise at nadir will be increased higher than that at edge if the fixed γ, i.e. the same amount of penalty, is placed on the noise term in (4) for all the scan positons. Since in NWP, a stable noise estimate (NEDT) of the sensors is required to establish the measurement error covariance matrix [33], the FOV-dependent feature of noise may hinder the applications of the remapping data in this field.

To address this issue, in this study, the noise-tuning parameter γ is selected based on tradeoff curves to ensure a stable noise level in the entire reconstructed image. The tradeoff curves are expressed as the noise amplification ratio $\sigma_{target}/\sigma_{source}$ vs normalized fit error Q_1:

$$Q_1 = Q_0/\int G_{target}(\rho)^2 \ dA \tag{5}$$

Specifically, given a certain value of γ, minimizing the objective function (4a) yields coefficients that can be used to calculate Q_1 from (4b)-(5) and $\sigma_{target}/\sigma_{source}$ from (3). By varying γ from 0° to 90°, a series of samples of (Q_1, $\sigma_{target}/\sigma_{source}$) corresponding to various γ can be obtained. The tradeoff curve is then plotted from these samples with Q_1 as its x-axis and $\sigma_{target}/\sigma_{source}$ as its y-axis. This curve is plotted for each scan position. The optimum value of γ is selected at the point of the curve where the noise amplification ratio reach the same prescribed value for all the FOVs. The noise amplification ratio consistent along the scan line ensures a stable noise level in the reconstructed data set.

III. SIMULATION RESULTS

To objectively specify the optimum parameters and validate the performance of the new algorithm, it is helpful to use simulation. In this study, *Ta* observed with the source and target antenna pattern are simulated following the procedure described in [7]. In brevity, the PSF at each FOV is generated by projecting the antenna pattern onto the earth's surface based on ATMS instrument scan geometry. Brightness temperature within the PSF are simulated by the Community Radiative Transfer Model (CRTM) for the atmosphere and surface geophysical parameters provided by the Global Forecast System (GFS) with a 0.12° grid resolution. Antenna temperature is generated from the convolution of *Tb* with the PSF. For the source observations of channel 1, Gaussian white noise with the standard deviation equal to the NEDT of channel 1, 0.22 K, is added. The reconstruction algorithm is then applied to the simulated source measurements to generate the remapped results. The remapped and target data are compared to make a quantitative evaluation of the remapping algorithm.

In this section, the case of Hurricane Dorian at 18:00 UTC 31 August 2019 is adopted for the evaluation. The simulation of the NOAA-20 ATMS observations with the source and target antenna patterns are presented in Fig. 2 (a-b). Fig. 2 (c-d) shows the remapped results using the fixed 3×3 window and the adaptive window with optimum parameters. The process to select these optimum parameters will be elaborated in Section III-A and III-B. Fig. 2 (e-f) illustrates the difference between the remapped and the target data. It clearly shows that, compared to the fixed window, the adaptive window method can

gain much higher spatial resolution at coastlines and hurricane centers, and significantly reduce the bias stemming from the resolution difference. The quantitative evaluation of the effectiveness of the new algorithm will be detailed in the Section III-C and III-D.

A. Selection of the Optimum Noise-tuning Parameter

As described in Section II-B, the optimum value of the noise-tuning parameter γ is specified through the tradeoff curve at each scan position. Note that this method is applicable to any window types. In this section, the adaptive window with -5 dB threshold is adopted as an example to illustrate the procedure of this new method. Examples are shown in Fig. 3 to illustrate the behavior of the tradeoff curves at the scan edge and nadir. The curves at other scan positions share the similar features. In each case, two curves are shown, one for the 3×3 window and one for the adaptive window. The gross behavior of the tradeoff curves is the same. The noise amplification ratio $\sigma_{target}/\sigma_{source}$ decreases monotonically with increasing Q_1. The decrease is rapid at small values of Q_1, followed by a leveling off with its increasing value. The left end point of the curve with the maximum noise amplification and minimum fit error corresponds to a choice of γ=0° in (4a), while the opposite end of the curve which has the minimum noise and maximum fit error corresponds to a choice of γ=90°. To obtain a good remapping accuracy, the steep portion of the tradeoff curves is of greater practical interest. Fig. 3 shows that the steep portion of the curve shifts in the direction of decreasing Q_1 as the window switch from the fixed 3×3 to the adaptive one. Therefore, for a given value of remapping accuracy Q_1, the image reconstructed by

adaptive window has much lower noise than that produced by the fixed 3×3 window, while for a given value of the noise $\sigma_{target}/\sigma_{source}$, the adaptive window can achieve higher spatial resolution than the 3×3 window. Compared to the tradeoff curves at scan edge (Fig. 3 (a)), the curves at nadir (Fig. 3 (b)) have relatively higher dynamic range. This is because ATMS channel 1 FOV size is much smaller at nadir than at edge which allows the reconstruction at nadir to reach higher degree of spatial resolution enhancement as well as higher increase in noise.

As illustrated by the tradeoff curves, to have a low fit error, the noise amplification ratio needs to be set as high as possible within an acceptable level. In this paper, the NEDT specification for NOAA-20 ATMS channel 1, 0.7 K, is regarded as an upper limit for the remapping uncertainties [16]. To ensure a stable and acceptable noise level, γ is selected at the tradeoff curve for each FOV where the noise amplification ratio equals to 2.5 (i.e. the crosses on the curves in Fig. 3). As will be shown in Section III. D, this setting restricts the uncertainties of remapping results under the sensor's NEDT specification limit.

Fig. 4 presents the noise level (left panel) and the derived coefficients (right panel) when γ is fixed to 0.116° (lower panel) and determined by the tradeoff curves (upper panel). Fig. 4 (a) shows that the strategy proposed in this study leads to a FOV-dependent γ which ensures a constant noise level across the scan line. Fig. 4 (c) shows that a fixed γ leads to an evident increase in noise from scan edge to nadir. This can be explained by (3) and the derived coefficients presented in Fig. 4 (b) and (d).

According to (3), given a specific sensor with a certain NEDT, the noise level in the reconstructed data solely depends on the variance of the BGI coefficients. As showed in Fig. 4 (d), when γ is fixed for all the FOV positions, the variance of the coefficients for the FOV at nadir is larger than that at scan edge. This leads to the variation of the noise along scan. When γ is determined by the new strategy, the variance of the coefficients for the FOV at nadir is similar to that at edge (Fig. 4 (b)). This results in the same noise level along scan.

For a more intuitive comparison, the coefficients derived by the FOV-dependent γ and the fixed γ in Fig. 4 are applied to the simulated data set. The difference between the reconstructed result and the simulated truth are presented in Fig. 5. In addition, the bias and Standard Deviation (STD) of the error at each FOV position are calculated and presented in Fig. 6. Fig. 5 and Fig. 6 show that the remapping result with the fixed γ has much higher noise around nadir than scan edge, and this feature is not evident in the image reconstructed with the FOV-dependent γ. The overall error statistics are listed in Table I. The numbers show that the remapping result from the adaptive window with fixed γ and FOV-dependent γ have similar bias but the former window produces higher STD and RMS error than the later one. The features of the noise distribution are consistent with what is showed in Fig. 4.

The simulation results are consistent with what we expect in Section II-B. By fixing the noise amplification ratio over scan, γ is automatically adjusted to lay more penalty on

the noise term at nadir and less penalty at edge. This counteracts the FOV-dependent feature of the noise caused by the sensor's cross-scanning manner.

B. Selection of the Optimum Adaptive Window

As described in Section II-A, the adaptive window with a specific gain threshold is used in this study to provide BGI algorithm with more sub-footprint information. This strategy allows the source observations to be engaged in the reconstruction only if their antenna gain at the target FOV exceeds a certain threshold. In this section, the optimum threshold of the adaptive window is determined through simulations.

Fig. 7 presents the window size at nadir and the Root-Mean-Square error (RMS) calculated from the difference between the "truth" and the remapped results with various window types. This is performed for the fixed 3×3 window and the adaptive windows with the threshold varying from 0 dB to -13 dB below the peak gain. It shows that, with the adaptive window, many more measurements are employed in BGI algorithm than the fixed 3×3 window. The window size increases quickly with the decrease of the threshold. The RMS drops sharply when switching form the fix 3×3 window to the adaptive window with 0 dB threshold. As the threshold continues to decrease, the RMS first slightly fluctuates and then stays steady at around 0.65 K where the threshold is below -5 dB.

The deviation from the remapping results to the simulated truth for the first five adaptive windows are presented in Fig. 8. It can be seen that enlarging the adaptive window from 0 dB to -3 dB effectively reduces the error around the coastline area. The

window with -5 dB threshold has slightly better performance along the north coastline of Cuba than the -3 dB window. Further decreasing the threshold below -5 dB makes not much improvement in the results.

Comparing to the 3×3 window, the large size and irregular shape of the adaptive window leads to extra process time. For the Hurricane Dorian case showed in Fig. 2, the process time of the 3×3 window and the adaptive window with -5 dB threshold on the Red Hat Linux 6.0 server with a single Inter Xeon CPU (2.5 GHz frequency and 128 G memory) is 0.6 s and 6 s respectively. Considering using the multi-core parallel computing in the future, the extra computational time caused by the complexity of the adaptive window will not be an issue for its operational application.

This experiment demonstrates that the adaptive window with -5 dB threshold is large enough to provide sufficient information for remapping and the computational time is acceptable for the operational practice. Therefore, the adaptive window with this threshold is regarded as the optimum choice.

C. Reconstruction of the Point Spread Function (PSF)

The PSF describes the spatial characteristics of the antenna gain projected on the earth surface. Analysis of the PSF is helpful to validate the remapping accuracy. According to the objective function (4b), the reconstructed PSF can be straightly expressed as the sum of the source PSF weighted by its corresponding coefficient. With the BGI coefficients generated with the optimum parameters, the source, synthetic, and the target PSFs along with their Fourier transform spectrum are calculated and presented

in Fig. 9. The comparison of the results in the spatial domain (upper panel of Fig. 9) shows that the PSF reconstructed with the adaptive window has a more prominent center and a narrower beam width than the one produced by the conventional 3×3 window. In the frequency domain (lower panel of Fig. 9), it is clearly showed that the PSF built from 3×3 window is only able to recover very limited low frequency components, while the PSF built from adaptive window provides much richer information at high frequencies. Although compared to the target PSF, the one generated by adaptive window has slightly higher amplitude at low frequency and lower amplitude at high frequency, the improvement relative to the fixed 3×3 window is evident.

To quantitatively evaluate the remapping accuracy, the beam widths of the response functions before and after correction are estimated based on the PSFs in spatial domain. To do so, the half-power points of the PSFs are extracted and fitted by a circular curve, as is showed in Fig. 10. From the FOV size, i.e. the diameter of the circle and the altitude of the satellite (824 km for NOAA-20), the beam widths can be obtained. Results show that the BGI algorithm with 3×3 window is capable of narrowing the beam width from 5.3° to 4.5°. By using the adaptive window, the beam width can be further reduced to 4.0°. The improvement is increased from 15% to 25%.

D. Quantitative Validation of the New Algorithm

The simulation of the Hurricane Dorian case is used in this section to quantitatively evaluate the effectiveness of the new method. As is showed in Fig. 2, compared to the

image generated by the 3×3 window (Fig. 2 (c)), the one produced by the adaptive window (Fig. 2 (d)) exhibits much clearer coastlines and more details around the hurricane center. These features are closer to the simulated truth (Fig. 2 (b)). The deviation from the remapped image to the truth are presented in (Fig. 2 (e-f)). The error image of the 3×3 window shows obvious positive bias over water and negative bias over land around the islands, whereas on the error image of the adaptive window, such error pattern has been almost eliminated. This indicates that the issue of the insufficient resolution enhancement has been largely solved by using the adaptive window method. However, the comparison of Fig. 2 (e) and (f) also shows that the image produced from adaptive window has relatively larger negative error at the rightmost column than the 3×3 window. The explanation to this issue and the possible solution will be laid out in the next section.

Error statistics (mean, Standard Deviation (STD), and Root Mean Square (RMS)), computed from the difference between the "truth" and the observations before and after the remapping process, are given in Table I. The numbers suggest that the BGI with 3×3 window is capable of reducing the STD but leave the bias almost unchanged. In comparison, the adaptive window method manages to effectively eliminated the bias to zero and further reduces the STD from 1.49 K to 0.65 K, which is under the NOAA-20 ATMS channel 1's NEDT specification [16]. The fact that the image reconstructed with adaptive window has its STD and RMS (0.65 K) close to the amplified noise σ_{target} (0.55 K) calculated by (3), suggests that the noise, rather than the fit error, makes the major contribution to the remapping error. This indicates that the strategy to determine

the noise tuning parameter proposed in this study is a necessity to guarantee a consistent noise level for the overall reconstructed image. With the fixed 3×3 window, the overall RMS decreases by 40% compared to the raw data while with the adaptive window, this number decreases as much as 70%. This experiment demonstrates that using adaptive window in BGI algorithm can effectively increase the amount of information and significantly improve the spatial resolution while maintaining the noise level at an acceptable level.

E. The Underperformance of the Adaptive Window Method at Scan Edge over Uniform Antenna Temperature Area

As mentioned in the previous section, comparing to 3×3 window, the adaptive window has relatively larger negative bias at the right edge of the scan line. This issue can be explained by the insufficiency of the data in adaptive window at scan edge and the slowly varying Ta at the right part of the simulated area.

Firstly, the performance of the adaptive window at scan edge is not as good as that at nadir. Comparing the tradeoff curves of the adaptive window at nadir and at scan edge (solid lines in Fig. 3), with the same noise amplification ratio 2.5, the adaptive window has slightly higher value of Q_1 at scan edge than at nadir, indicating a larger fit error at scan edge. This is due to the ATMS's cross-track scanning manner which makes it impossible to have adequate observations fully cover the pixel of interest at scan edge. As showed in Fig. 1, the source observations only cover about half of the pixel of interest at the outmost scan positions.

Secondly, the signal's slowly varying pattern benefits the small window. As it is known, when dealing with uniform Ta field, antenna pattern has no impact on the output, i.e. the Ta observed by source and target antenna pattern would be the same and equal to the Tb of this area. This is exactly what BGI does when its window covers uniform observations. According to (2), since the uniform Ta can be moved out of the sum and the sum of the coefficients is unity, the reconstructed Ta exactly equals to the source one. In this scenario, the synthetic antenna pattern, no matter how inaccurate it is, will have no impact on the result. BGI degenerates into the direct assignment of the source Ta. Therefore, for the signal slowly varying area, the small window containing uniform observations tends to make better prediction.

Zooming into the rightmost FOV of the 18th scan line, Fig. 11 shows the source observations involved in the adaptive window and the 3×3 window. It can be seen that the 3×3 window covers small area and the source Ta within it appears uniform. Thus, the remapping result tends to be the average of Ta within the window. Conversely, the adaptive window covers much larer area and the observations within it has much lower value at the left part than at the target FOV. Since the beam width of the synthetic antenna pattern is larger than the target one, the Ta at the left part of the window 'seen' by the sythetic antenna, but not by the target one, will have negative impact on the remapping result. The calculation shows that the target Ta is 251.2 K. While the prediction error of the 3×3 window is 0.05 K, the synthetic Ta from the adaptive window is 2 K below the truth.

One thing we want to point out is that the underperformance of adaptive window at the rightmost FOV doesn't mean that its synthetic antenna pattern is worse than that created by the 3×3 window. On the contrary, the tradeoff curves in Fig. 3 and the outperformace of adaptive window at the left part of the simulation where signal changes sharply (Fig. 2) demonstrates that the synthetic antenna pattern created by adaptive window is much more accurate than that by 3×3 window. The underperformance of the adaptive window observed at the rightmost columns is the combined effect of the insufficiency of the data in adaptive window at scan edge and the slowly varying antenna temperature at that area.

It is also noticeable in Fig. 2 (f) that at the signal slowly varying area other than the rightmost part, the performance of adaptive window is similar to that of the 3×3 window. This suggests that with more observations fully covering the pixel of interest at scan edge, the adaptive window can reach higher fit accuracy and the issues for uniform Ta field observed at scan edge can be addressed. A possible solution is to combine the data from the adjacent orbits into the reconstruction of the PSF at scan edge, as the CETB system did to converse the swath-based satellite data to the regular grid with high spatial resolution [3]-[5] . However, the difference in these observations caused by more than 100 minutes time interval between NOAA-20 adjacent orbits can be significant. This difference will impact the accuracy of the reconstruction and needs to be taken into consideration. Since the area with sharply changing signal, such as hurricane centers, is of greater interest to scientific community and the ATMS operational resampling requires real-time process, combining the observations from multiple orbits to improve

the remapping accuracy at scan edge for uniform Ta field will not be carried out in this study.

IV. REAL ATMS DATA RESULTS

Having selected the optimum noise-tuning parameter, γ, and adaptive window threshold based on simulation, in this section, we validate the performance of the new algorithm with the real ATMS data. Fig. 12 shows the raw observations and remapping results of NOAA-20 ATMS channel 1 for Hurricane Dorian over North Atlantic Ocean at 18:00 UTC 31 August 2019 captured by the ascending orbit. The remapping results (Fig. 12 (b-c)) demonstrate that compared with the 3×3 window result, the image generated with the adaptive window uncovers more detailed structures not only around the hurricane center and coastlines where the signal change sharply, but also near the scan edge where the signal's variation is relatively weak. Since the truth is unavailable for the actual case, the deviation from the remapped result to the raw data is computed (Fig. 12 (d-e)) to illustrate the degree of the spatial resolution enhancement. The comparison shows that the resolution enhancement achieved by the adaptive window is much higher than that can be obtained by the 3×3 window. Focusing on the coastline of Cuba, the difference between the raw data and the data remapped with the 3×3 window (Fig. 12 (d)) gradually disappears as the scan angle increases, whereas this pattern is not observed in the image remapped by the adaptive window (Fig. 12 (e)).

Fig. 13 presents the case of typhoon Surigae near Philippines at 17:00 UTC 19 April 2021 caught by ATMS during its descending orbit. The figure shows that, comparing to the 3×3 window result, the image produced by the adaptive window unfolds more details of the typhoon structure and more distinct coastlines. Both Fig. 14 and Fig. 15 display the clear sky image of the South America. While Fig. 14 focuses on the Amazon River Delta region located around the Equator, Fig. 15 shows the southern part of the continent stretching from 15°S to 60°S. It can be seen that the adaptive window gains much higher spatial resolution along the tributaries of the Amazon river than the 3×3 window. Both figures suggest that the adaptive window has similar remapping accuracy along the scan line while the 3×3 window has lower accuracy around the scan edge.

The above cases covering different weather conditions and regions lead to the same conclusions. The spatial resolution enhancement capability of the 3×3 window deteriorates as the scan angle increases. With the adaptive window, the degree of the resolution enhancement stays high across the entire scan line. The experiments indicate that the information provided by the fixed window is insufficient for the accurate remapping and this issue can be effectively alleviated by the adaptive window method.

V. CONCLUSION

The intrinsic antenna pattern match for the observations from multiple space-borne microwave sensors is the premise for their accurate applications in various data fusion techniques. The well-established Backus-Gilbert Inversion (BGI) algorithm has long been adopted for the Advanced Technology Microwave Sounder (ATMS) remapping.

However, although the spatial resolution degradation by BGI is near-perfect, the resolution enhancement still needs to be improved. This study revealed that the root cause is the insufficiency of the information provided by the conventional fixed reconstruction window. To improve the spatial resolution enhancement accuracy, the adaptive window method is applied to increase the amount of sub-footprint scale information. In addition, a new noise tuning method is proposed to eliminate the FOV-dependent features of the noise in the remapped images caused by the sensor's cross-track scanning manner.

To evaluate the effectiveness of the new method, the BGI algorithm with the adaptive window and the conventional fixed 3×3 window are applied to remap ATMS channel 1 data with 5.2° beam width to the AMSU-A like 3.3° beam width. The numerical results from simulated data sets and real satellite observations show that the adaptive window method can significantly improve the spatial resolution enhancement accuracy while maintaining the noise level at an acceptable level. Compared to the fixed window, the new method narrows the beam width of the antenna pattern by 10%. The bias stemming from the spatial resolution differences is reduced to 0 K and the overall RMS is declined by 30%. The issue of the deterioration of the resolution enhancement capability near the scan edge when using the fixed window has been largely ameliorated by the adaptive window method. With the FOV-dependent noise-tuning parameters specified through the trade-off curves, the noise level is suppressed steadily at 0.6 K over scan. However, the adaptive window has relatively low remapping accuracy at scan edge when dealing with uniform antenna temperature area. A possible solution to

this issue is to combine the data from the adjacent satellite orbits into the reconstruction at scan edge.

The improved BGI algorithm proposed in this paper can be easily applied to other spaceborne microwave sensors. It should be noted that the spatial resolution enhancement required in ATMS remapping from 5.2 ° to 3.3 ° beam width is mild. In this scenario, the noise, rather than the fit error, dominates the remapping uncertainties. The noise-tuning method proposed in this study can effectively make the noise, the major component in the remapping uncertainties, acceptable and consistent along the scan line. However, for higher spatial resolution enhancement when fit error becomes dominant in the remapping uncertainties, the noise-tuning method that determines the parameter solely from tradeoff curves may not be applicable. In that case, to ensure an acceptable and consistent noise level over scan line, the noise-tuning parameter needs to be selected for each FOV or each group of the neighboring FOVs through simulations.

Another advantage of the adaptive window over the fixed window is its capability of dealing with the irregular sampled data, like the measurements from small satellite constellation and the observations combined from multiple passes of a single spacecraft system. Future work will focus on processing these measurements through the improved BGI algorithm, with the purpose of producing high quality microwave data with finer spatial resolution and lower noise level. The software package of the new algorithm developed in this paper is publicly available at https://github.com/JunUMD/BG_AdaptiveWindow_v1.git

Acknowledgements. The authors would like to thank Prof. David G. Long and Dr. Harrison Garrett from the Brigham Young University, Provo, UT USA for the insightful discussions over the BGI algorithm. Review comments from the anonymous reviewers are greatly appreciated.

REFERENCES

[1] W. D. Robinson, C. Kummerow, and W. S. Olson, "A technique for enhancing and matching the resolution of microwave measurements from the SSM/I instrument," *IEEE Transactions on Geoscience and Remote Sensing,* vol. 30, no. 3, pp. 419-429, 1992.

[2] A. Stogryn, "Estimates of brightness temperatures from scanning radiometer data," *IEEE Transactions on Antennas and Propagation,* vol. 26, no. 5, pp. 720-726, 1978.

[3] D. G. Long, and D. L. Daum, "Spatial resolution enhancement of SSM/I data," *IEEE Transactions on Geoscience and Remote Sensing,* vol. 36, no. 2, pp. 407-417, 1998.

[4] D. G. Long, M. J. Brodzik, and M. A. Hardman, "Enhanced-resolution SMAP brightness temperature image products," *IEEE Transactions on Geoscience and Remote Sensing,* vol. 57, no. 7, pp. 4151-4163, 2019.

[5] D. G. Long, and M. J. Brodzik, "Optimum image formation for spaceborne microwave radiometer products," *IEEE Transactions on Geoscience and Remote Sensing,* vol. 54, no. 5, pp. 2763-2779, 2016.

[6] H. Yang, and X. Zou, "Optimal ATMS remapping algorithm for climate research," *IEEE Transactions on Geoscience and Remote Sensing,* vol. 52, no. 11, pp. 7290-7296, 2014.

[7] J. Zhou, and H. Yang, "Comparison of the remapping algorithms for the Advanced Technology Microwave Sounder (ATMS)," *Remote Sensing,* vol. 12, no. 4, pp. 672, 2020.

[8] N. Atkinson, *Annex to AAPP scientific documentation: Preprocessing of ATMS and CrIS*, EUMESAT and the Met Office, Devon, UK, 2011.

[9] G. Backus, and J. F. Gilbert, "Numerical applications of a formalism for geophysical inverse problems," *Geophysical Journal International,* vol. 13, no. 1-3, pp. 247-276, 1967.

[10] G. Backus, and F. Gilbert, "The resolving power of gross earth data," *Geophysical Journal International,* vol. 16, no. 2, pp. 169-205, 1968.

[11] G. Backus, F. Gilbert, and E. C. Bullard, "Uniqueness in the inversion of inaccurate gross Earth data," *Philosophical Transactions of the Royal Society of London. Series A, Mathematical and Physical Sciences,* vol. 266, no. 1173, pp. 123-192, 1970/03/05, 1970.

[12] P. C. Hansen, "The Backus-Gilbert method: SVD analysis and fast implementation," *Inverse Problems,* vol. 10, no. 4, pp. 895-904, 1994/08/01, 1994.

[13] P. J. Stephens, and A. S. Jones, "A computationally efficient discrete Backus-Gilbert footprint-matching algorithm," *IEEE Transactions on Geoscience and Remote Sensing,* vol. 40, no. 8, pp. 1865-1878, 2002.

[14] T. Himani, and A. S. Jones, "Microwave resolution enhancement using distributed small spacecraft architectures," *IEEE Transactions on Geoscience and Remote Sensing*, pp. 1-11, 2020.

[15] H. Yang, J. Shang, L.-q. Lu *et al.*, "Study of channel resolution matching of spaceborne microwave radiometer and its application in MWRI of FY-3 satellite," *Aerosp. Shanghai,* vol. 29, no. 1, pp. 23-28, 2012.

[16] NOAA, *Joint Polar Satellite System (JPSS) Advanced Technology Microwave Sounder (ATMS) SDR Calibration Algorithm Theoretical Basis Document (ATBD)*, Center for Satellite Applications and Research, College Park, MD, USA, 2013.

[17] X. Zou, and X. Tian, "Hurricane warm-core retrievals from AMSU-A and remapped ATMS measurements with rain contamination eliminated," *Journal of Geophysical Research: Atmospheres,* vol. 123, no. 19, pp. 10,815-10,829, 2018/10/16, 2018.

[18] T. Hu, F. Zhang, W. Li *et al.*, "Microwave radiometer data superresolution using image degradation and residual network," *IEEE Transactions on Geoscience and Remote Sensing,* vol. 57, no. 11, pp. 8954-8967, 2019.

[19] W. Hu, W. Zhang, S. Chen, X. Lv, D. An, and L. Ligthart, “A deconvolution technology of microwave radiometer data using convolutional neural networks,” *Remote Sens.*, vol. 10, no. 2, p. 275, Feb. 2018.

[20] W. Hu, Y. Li, W. Zhang, S. Chen, X. Lv, and L. Ligthart, “Spatial resolution enhancement of satellite microwave radiometer data with deep residual convolutional neural network,” *Remote Sens*., vol. 11, no. 7, p. 771, Mar. 2019.

[21] Y. Li et al., “Spatial resolution matching of microwave radiometer data with convolutional neural network,” *Remote Sens*., vol. 11, no. 20, p. 2432, Oct. 2019.

[22] T. Hu, F. Zhang, W. Li, W. Hu, and R. Tao, “Microwave radiometer data superresolution using image degradation and residual network,” *IEEE Trans. Geosci. Remote Sens.*, vol. 57, no. 11, pp. 8954–8967, Nov. 2019.

[23] K. Chen, X. Fan, W. Han and H. Xiao, "A Remapping Technique of FY-3D MWRI Based on a Convolutional Neural Network for the Reduction of Representativeness Error," in *IEEE Trans. Geosci. Remote Sens.*, vol. 60, pp. 1-11, 2022, Art no. 5302511, doi: 10.1109/TGRS.2021.3138395.

[24] J. Zhou and H. Yang, "Noise Suppression in ATMS Spatial Resolution Enhancement Using Adaptive Window Method," *2021 IEEE International Geoscience and Remote Sensing Symposium IGARSS*, 2021, pp. 7693-7695, doi: 10.1109/IGARSS47720.2021.9553997.

[25] M. Migliaccio, and A. Gambardella, “Microwave radiometer spatial resolution enhancement,” *IEEE Transactions on Geoscience and Remote Sensing,* vol. 43, no. 5, pp. 1159-1169, 2005.

[26] B. J. Conrath, “Vertical resolution of temperature profiles obtained from remote radiation measurements,” *Journal of Atmospheric Sciences,* vol. 29, no. 7, pp. 1262-1271, 01 Oct. 1972, 1972.

[27] C. D. Rodgers, *Inverse Methods for Atmospheric Sounding: Theory and Practice*: World scientific, 2012, pp. 65-79.

[28] M. R. Farrar, and E. A. Smith, “Spatial resolution enhancement of terrestrial features using deconvolved SSM/I microwave brightness temperatures,” *IEEE Transactions on Geoscience and Remote Sensing,* vol. 30, no. 2, pp. 349-355, 1992.

[29] R. Bennartz, “Optimal convolution of AMSU-B to AMSU-A,” J. Atmos. Ocean. Technol., vol. 17, no. 9, pp. 1215–1225, Sep. 2000.

[30] Technical report Backus-Gilbert footprint matching methodology applied on MWI and ICI observations TR/BG/MWI-ICI Issue 1.0, Rev. 1. June 5 2019.

[31] T. Maeda, Y. Taniguchi and K. Imaoka, "GCOM-W1 AMSR2 Level 1R Product: Dataset of Brightness Temperature Modified Using the Antenna Pattern Matching Technique," in IEEE Transactions on Geoscience and Remote Sensing, vol. 54, no. 2, pp. 770-782, Feb. 2016, doi: 10.1109/TGRS.2015.2465170.

[32] F. T. Ulaby, R. K. Moore, A. K. Fung, *Microwave Remote Sensing Active and Passive Volume I: Microwave Remote Sensing Fundamentals and Radiomerty:* Artech House, Jan 1, 1981, pp. 98-101.

[33] S. Boukabara, K. Garrett, W. Chen *et al.*, "MiRS: an all-weather 1DVAR satellite data assimilation and retrieval system," *IEEE Transactions on Geoscience and Remote Sensing,* vol. 49, no. 9, pp. 3249-3272, 2011.

TABLE I. ERROR STATISTICS FOR THE RAW AND REMAPPED OBSERVATIONS WITH THE 3×3 AND ADAPTIVE WINDOWS

Fig. 1. Reconstruction windows at the scan edge (a) and nadir (b). The blue circle denotes the pixel of interest, i.e. the outline of the projection of the target antenna pattern with 3.9 times its -3 dB beam width. The red and black crosses respectively represent the source ATMS channel-1 5.2° FOV centers in the 3×3 window and the adaptive window.

Fig. 2. Simulation results of ATMS channel-1 resolution enhancement from the source 5.2° FOV to the target 3.3° FOV. Simulated source (a) and target (b) observations; remapped observations with the 3×3 window (c) and the adaptive window (d); the deviation from the remapping results of the 3×3 window (e) and the adaptive window (f) to the simulated truth (remapping minus truth). Units are K.

Fig. 3. Tradeoff curves at the scan edge (a) and nadir (b). Solid and dashed lines are for the adaptive window and 3×3 window, respectively. The cross on each curve denotes the point where the noise amplification ratio is 2.5.

Fig. 4. The noise level and the BGI coefficients when γ is selected by the new method (upper panel) and fixed to 0.12 ° (lower panel). (a) and (c) show the value of γ (black) and the corresponding noise level (red) at each scan position. (b) and (d) show the BGI coefficients for the FOV at edge (blue) and nadir (black). The source observation index is shifted to make the one with the highest weight at center.

Fig. 5. The deviation from remapping results of the adaptive window with FOV-dependent γ (a) and fixed γ (b) to the simulated truth. Unit is K.

Fig. 6. Bias and STD error of the reconstruction from adaptive window with fixed γ (black line with grey shade) and FOV-dependent γ (red line with red shade).

Fig. 7. Window size at nadir (black) and the RMS error of the remapping results (red) for various window types, including the fixed 3×3 window and the adaptive window with the threshold from 0 dB to -13 dB.

Fig. 8. The deviation from the remapping results to the simulated truth for the adaptive windows with the gain threshold of 0, -1, -3, -5, -7 dB (a-e). Unit is K.

Fig. 9. The source, synthetic, and target PSFs at nadir. The source ATMS channel-1 PSF (a), the AMSU-A-like PSF reconstructed with the fixed 3×3 window (b) and the adaptive window (c), and the target AMSU-A PSF (d). (e–f) are the Fourier transforms of the PSFs (a–d). All response functions have been normalized to 1.0 to facilitate comparisons.

Fig. 10. Half-power points of the PSFs at nadir and their circular curve fittings. The black and green markers are for the source and the target PSFs, while the blue and red markers are for the synthetic PSFs with the fixed 3×3 window and the adaptive window respectively.

Fig. 11. Source data involved in the reconstruction of the target observation at the 95th FOV of 18th scan line. Colored points represent the antenna temperature of the data within the adaptive window and the black box circles the data used in the 3×3 window. Unit is K.

Fig. 12. Application of the BGI with the 3×3 window and the adaptive window to real ATMS observations of hurricane Dorian. (a) Raw observations of ATMS channel 1, (b)

3×3 window remapping result and (d) its difference from the raw data, (c) adaptive window remapping result and (e) its difference from the raw data. Units are K.

Fig. 13. The same as Fig. 12 but for the case of typhoon Surigae at 17:00 UTC 19 April 2021.

Fig. 14. The same as Fig. 12 but for the image of Amazon River Delta region.

Fig. 15. The same as Fig. 12 but for the image of Southern part of South America.

TABLE I

ERROR STATISTICS FOR THE RAW AND REMAPPED OBSERVATIONS

WITH THE 3×3 AND ADAPTIVE WINDOWS

Data	Bias (K)	STD (K)	RMS (K)
Raw	0.14	2.48	2.48
Remapped by 3×3 window	0.13	1.49	1.50
Remapped by adaptive window with fixed γ	0.05	0.93	0.93
Remapped by adaptive window with FOV-dependent γ	0.00	0.65	0.65

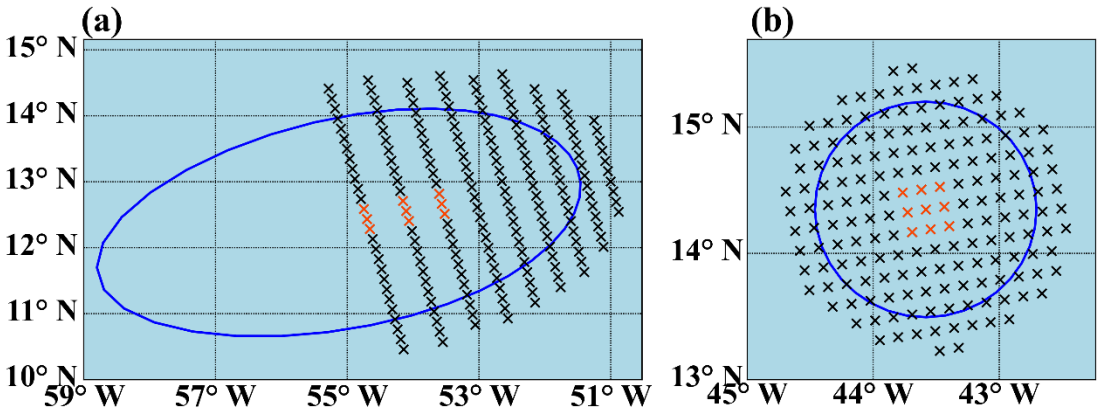

Fig. 1. Reconstruction windows at the scan edge (a) and nadir (b). The blue circle denotes the pixel of interest, i.e. the outline of the projection of the target antenna pattern with 3.9 times its -3 dB beam width. The red and black crosses respectively represent the source ATMS channel-1 5.2° FOV centers in the 3×3 window and the adaptive window.

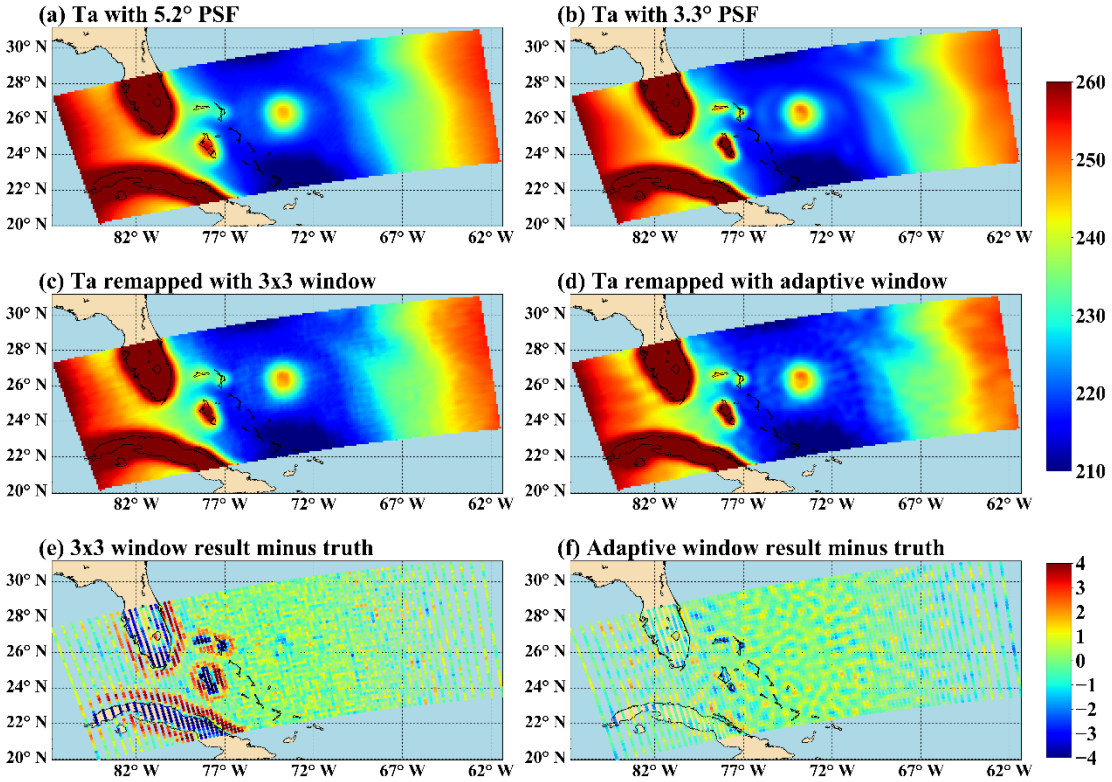

Fig. 2. Simulation results of ATMS channel-1 resolution enhancement from the source 5.2° FOV to the target 3.3° FOV. Simulated source (a) and target (b) observations; remapped observations with the 3×3 window (c) and the adaptive window (d); the deviation from the remapping results of the 3×3 window (e) and the adaptive window (f) to the simulated truth (remapping minus truth). Units are K.

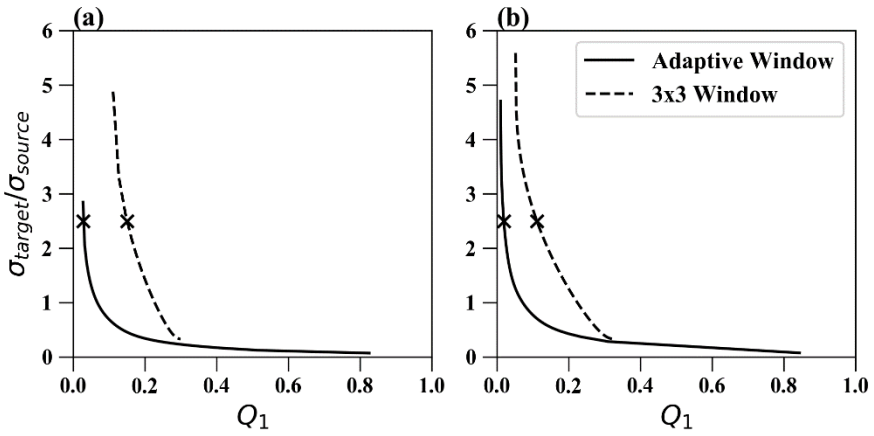

Fig. 3. Tradeoff curves at the scan edge (a) and nadir (b). Solid and dashed lines are for the adaptive window and 3×3 window, respectively. The cross on each curve denotes the point where the noise amplification ratio is 2.5.

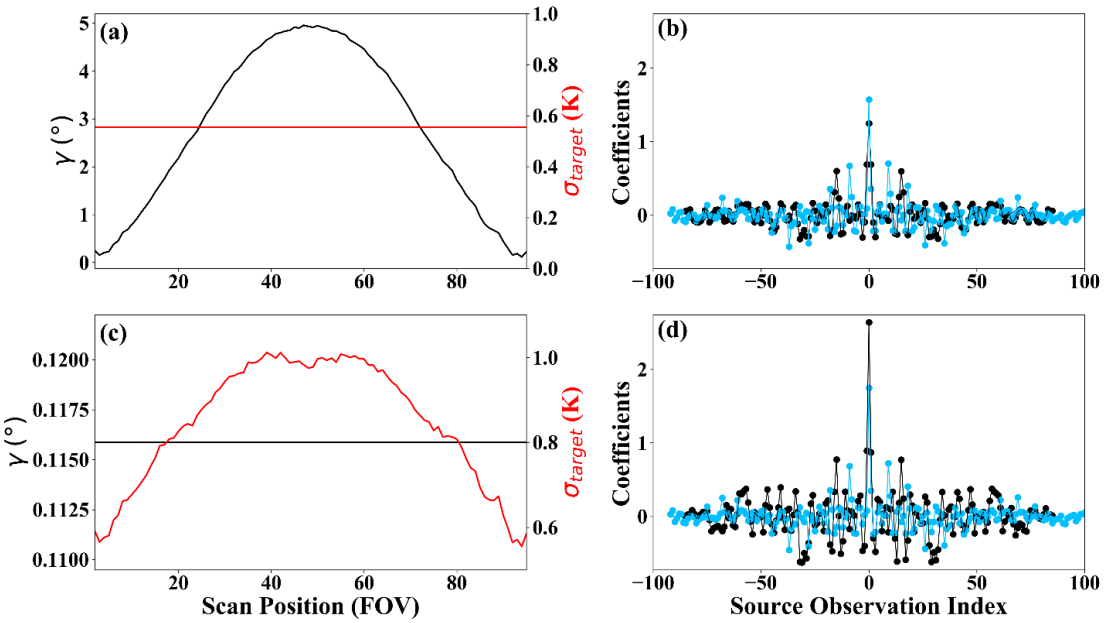

Fig. 4. The noise level and the BGI coefficients when γ is selected by the new method (upper panel) and fixed to 0.12 ° (lower panel). (a) and (c) show the value of γ (black) and the corresponding noise level (red) at each scan position. (b) and (d) show the BGI coefficients for the FOV at edge (blue) and nadir (black). The source observation index is shifted to make the one with the highest weight at center.

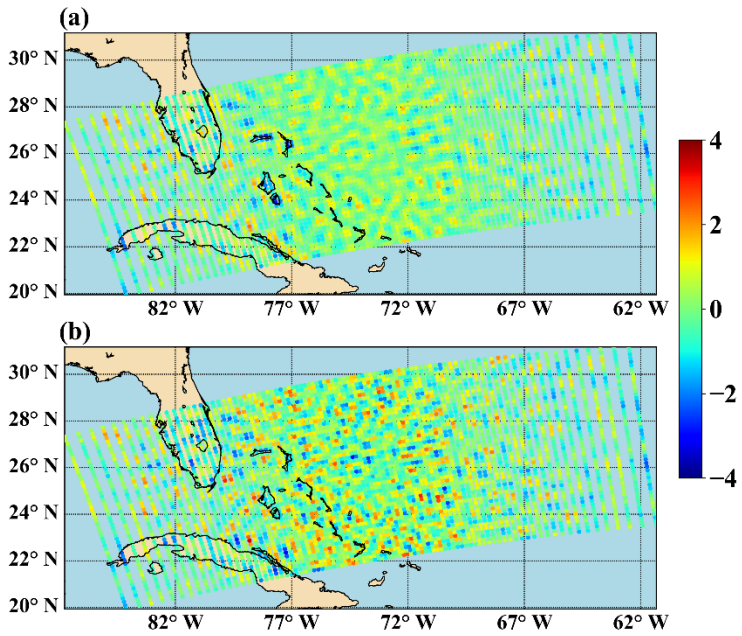

Fig. 5. The deviation from remapping results of the adaptive window with FOV-dependent γ (a) and fixed γ (b) to the simulated truth. Unit is K.

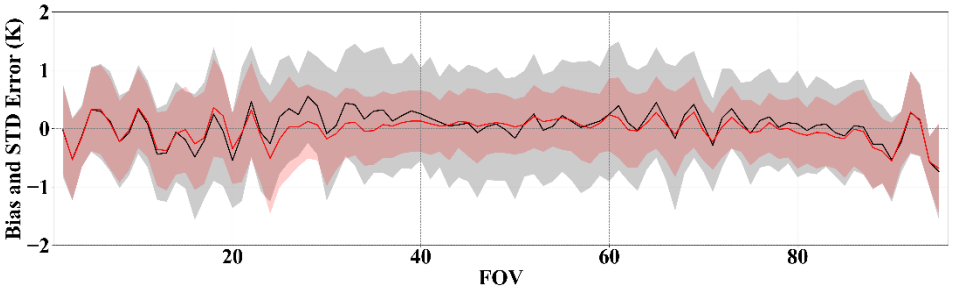

Fig. 6. Bias and STD error of the reconstruction from adaptive window with fixed γ (black line with grey shade) and FOV-dependent γ (red line with red shade).

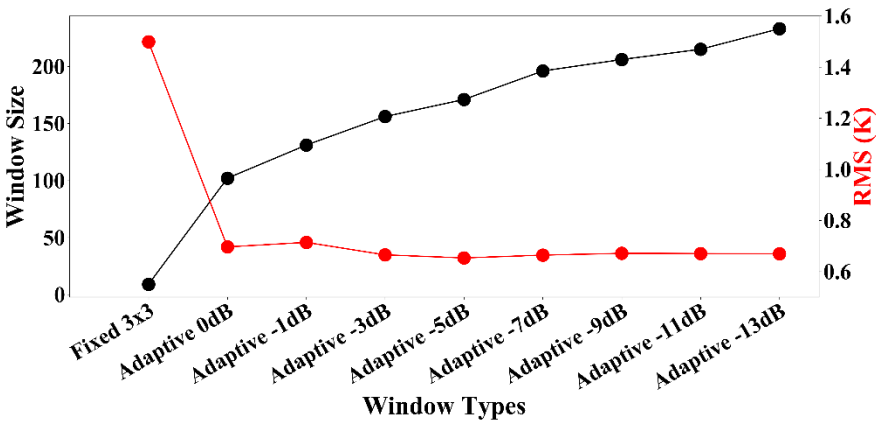

Fig. 7. Window size at nadir (black) and the RMS error of the remapping results (red) for various window types, including the fixed 3×3 window and the adaptive window with the threshold from 0 dB to -13 dB.

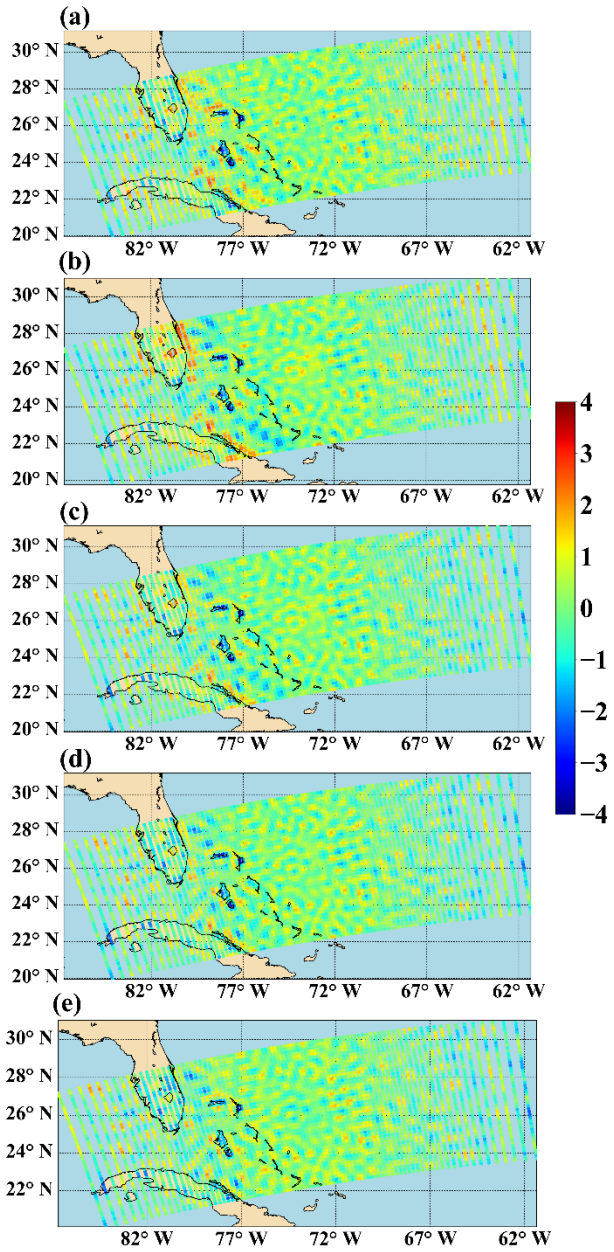

Fig. 8. The deviation from the remapping results to the simulated truth for the adaptive windows with the gain threshold of 0, -1, -3, -5, -7 dB (a-e). Unit is K.

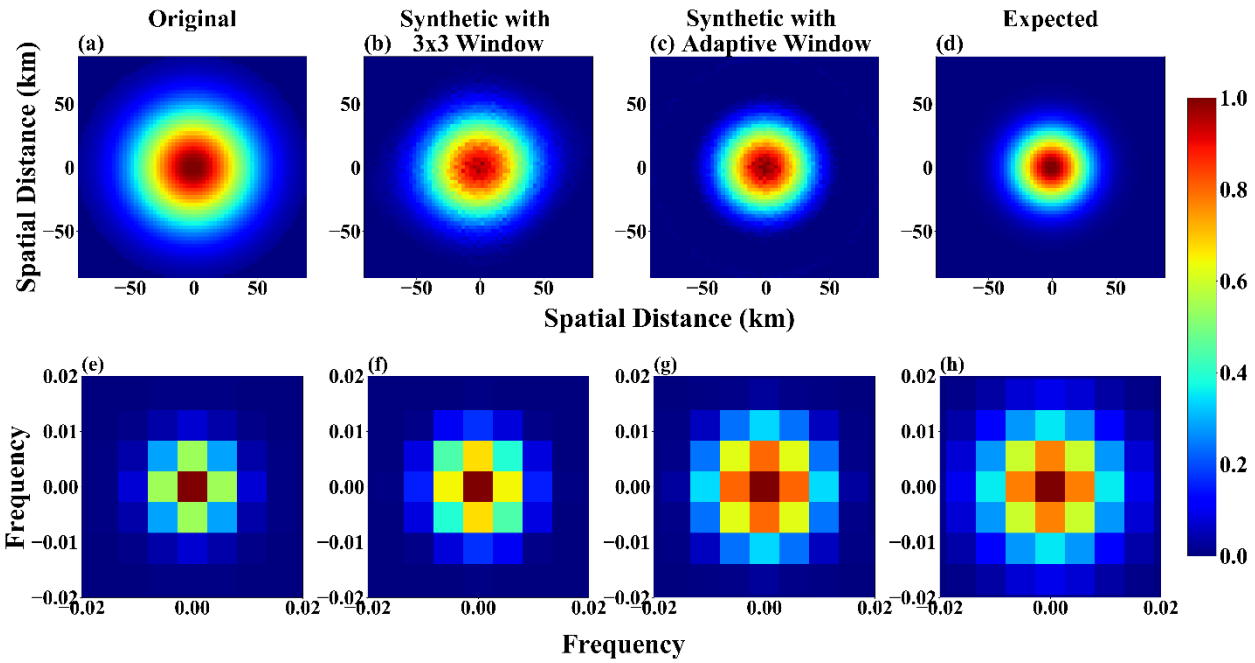

Fig. 9. The source, synthetic, and target PSFs at nadir. The source ATMS channel-1 PSF (a), the AMSU-A-like PSF reconstructed with the fixed 3×3 window (b) and the adaptive window (c), and the target AMSU-A PSF (d). (e–f) are the Fourier transforms of the PSFs (a–d). All response functions have been normalized to 1.0 to facilitate comparisons.

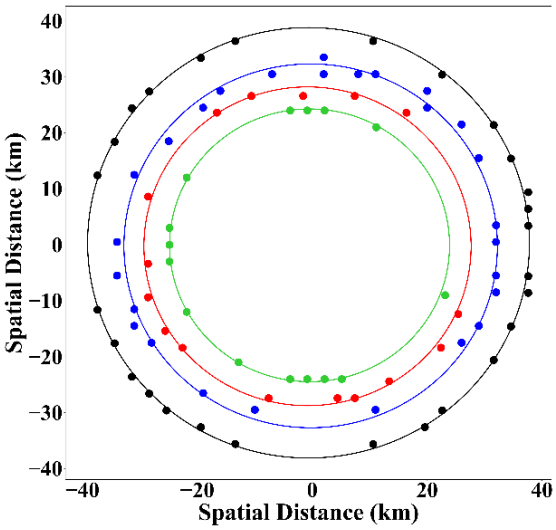

Fig. 10. Half-power points of the PSFs at nadir and their circular curve fittings. The black and green markers are for the source and the target PSFs, while the blue and red markers are for the synthetic PSFs with the fixed 3×3 window and the adaptive window respectively.

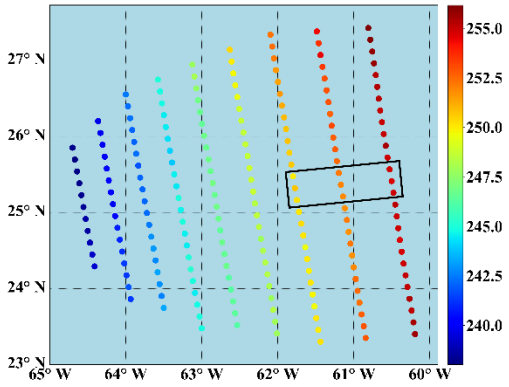

Fig. 11. Source data involved in the reconstruction of the target observation at the 95th FOV of 18th scan line. Colored points represent the antenna temperature of the data within the adaptive window and the black box circles the data used in the 3×3 window. Unit is K.

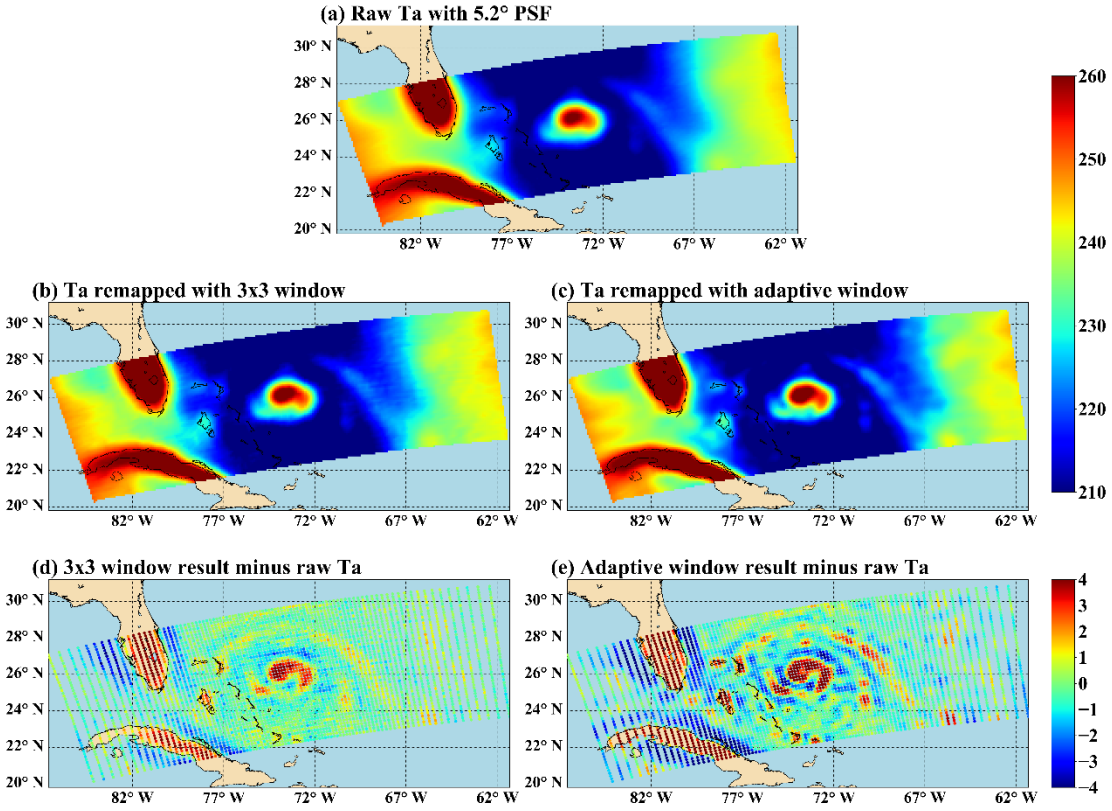

Fig. 12. Application of the BGI with the 3×3 window and the adaptive window to real ATMS observations of hurricane Dorian. (a) Raw observations of ATMS channel 1, (b) 3×3 window remapping result and (d) its difference from the raw data, (c) adaptive window remapping result and (e) its difference from the raw data. Units are K.

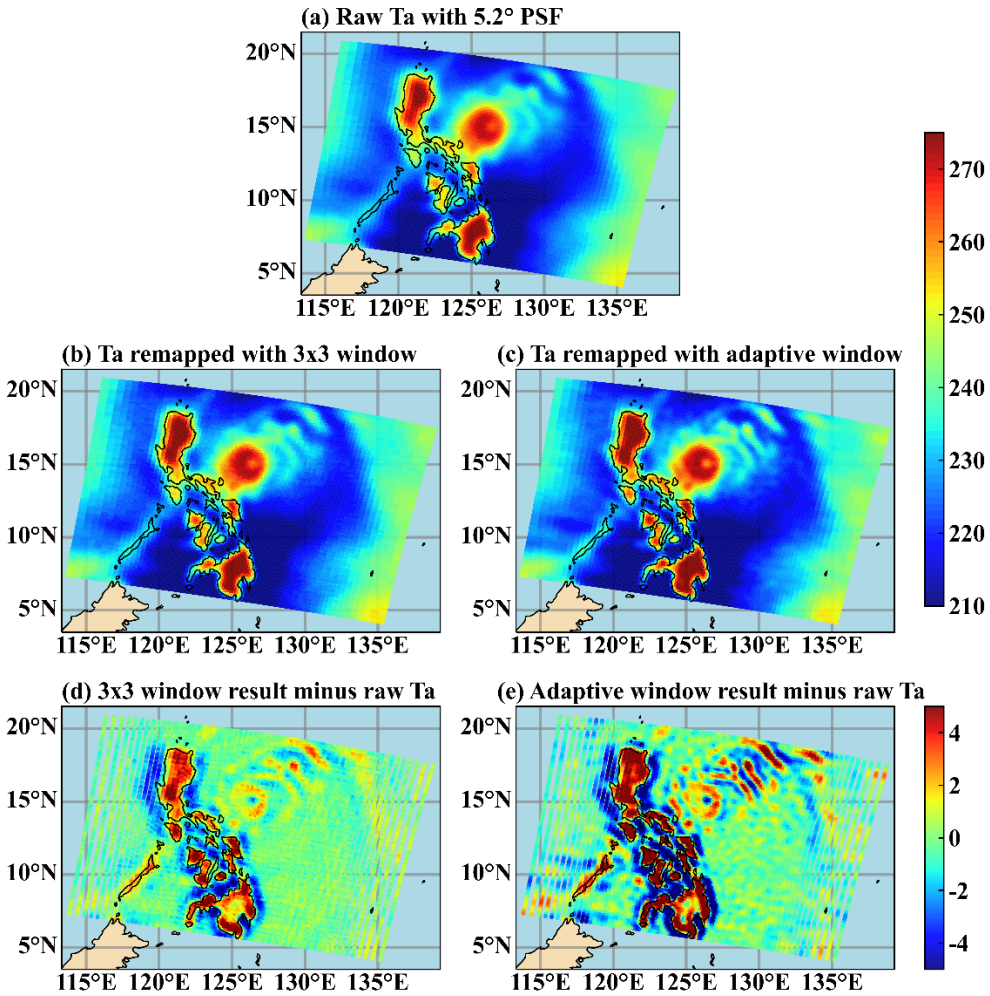

Fig. 13. The same as Fig. 12 but for the case of typhoon Surigae at 17:00 UTC 19 April 2021.

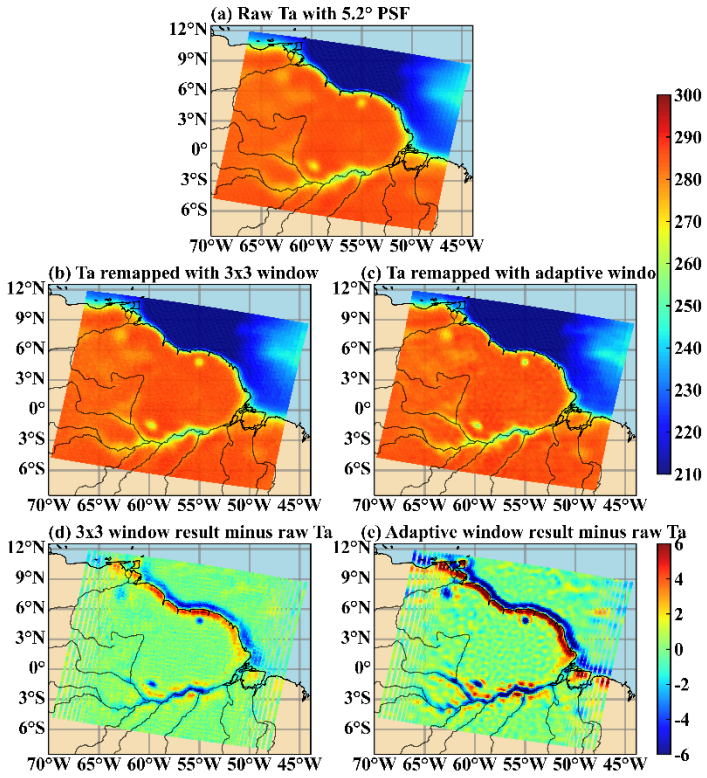

Fig. 14. The same as Fig. 12 but for the image of Amazon River Delta region.

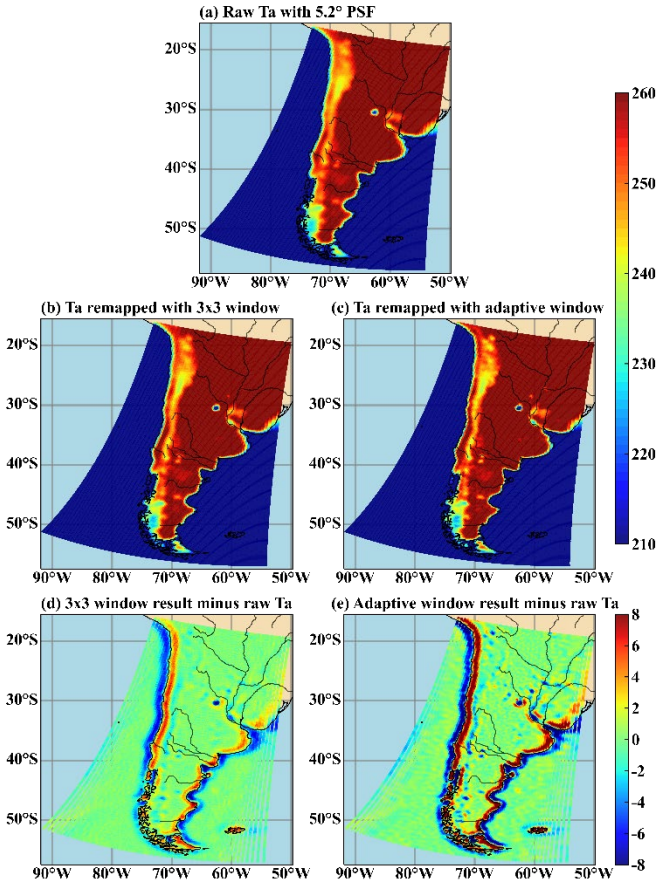

Fig. 15. The same as Fig. 12 but for the image of Southern part of South America.